IEEE Access
Multidisciplinary | Rapid Review | Open Access Journal

Received October 23, 2018, accepted November 25, 2018, date of publication December 11, 2018,
date of current version January 7, 2019.

Digital Object Identifier 10.1109/ACCESS.2018.2886196

Determination of Radiation Pressure in Acoustic Levitation by Optical Acoustic-Field Measurement

JAMES J. SCIRE, Jr., (Member, IEEE)
Department of Mechanical Engineering, New York Institute of Technology, Old Westbury, NY 11568, USA
e-mail: jscire@nyit.edu

This work was supported in part by the NYIT Office of Sponsored Programs and Research and in part by the Office of the Dean of the College of Engineering and Computing Sciences.

ABSTRACT Pulsed digital holography was used to determine the acoustic radiation force on objects suspended in a single-axis acoustic levitator. Digital holography provided both the object images and the optical phase data required to determine the instantaneous acoustic pressure. The phase data were utilized in tomography calculations, converting the measured line-of-sight variations to a pressure field by assuming that the system was axisymmetric. The pressure field was used to calculate the velocity field and these together were used to calculate the acoustic radiation pressure. This pressure was integrated over the surface of the object to determine the vertical force on the object. Force measurements were completed for five different polymer spheres, of different sizes and densities, and for an evaporating water droplet. For all but the heaviest sphere, the optically measured force agreed with the measured weight of the sphere within experimental uncertainty. For the heaviest sphere, the overall average showed an upward bias but was still only 4.7% high. For the water data, the optically measured force was consistent with the droplet volume as the droplet evaporated.

INDEX TERMS Acoustic measurements, holography, levitation, nonlinear acoustics.

I. INTRODUCTION

This paper describes the use of digital holography to measure the acoustic fields around small objects during acoustic levitation. From the field measurements, the acoustic radiation force on the object is calculated. By employing high-speed, pulsed holography, the force can be calculated even as the object moves during levitation.

Acoustic levitation is an important tool for manipulating and studying objects in situations where contact with surfaces cannot be permitted. Levitators employ high-amplitude acoustic standing waves to suspend objects near nodes. As the object moves away from the node, radiation pressure from the increasing acoustic field provides a restoring force. Shaping of the field around the nodes can provide both vertical suspension and horizontal containment of the object. In levitation and in other applications, the acoustic radiation force can also be used to manipulate objects by dynamically reshaping the acoustic field [1], [2].

Levitators do, however, exhibit complicated behavior. Instabilities can develop, causing the suspended object to oscillate or to be expelled [3], [4]. Suspended droplets can be shattered and bubbles can be formed in the liquid (e.g. [5]). This work was undertaken to determine whether digital holography could be a useful tool for the quantitative study of these phenomena. Here, we apply digital holography to determine the forces on objects of known mass or known density. By also tracking the motion of the objects using holography, we can determine how close the force calculations are to the forces calculated from the object motion. By examining the performance of the measurement technique in this way, we can determine how useful it will be for studying objects of unknown mass or density, such as bubbly liquid droplets.

We begin with background discussions of digital holography, acoustic radiation pressure, and prior work related to this study. We then give details of the experiments and calculation techniques. Finally, we report and discuss the results.

II. BACKGROUND

A. HOLOGRAPHY

Holography is a technique for the recording and reconstruction of full wavefronts, with both amplitude and phase. It has been used for a number of years in diverse fields such as flow visualization [6], the microscopic study of biological

2169-3536 © 2018 IEEE. Translations and content mining are permitted for academic research only.
Personal use is also permitted, but republication/redistribution requires IEEE permission.
See http://www.ieee.org/publications_standards/publications/rights/index.html for more information.

samples [7], and vibrational analysis. Conventional holography utilizes film as a recording medium, on which the interference between a reference beam and a coherent object beam are recorded. Reconstruction is performed by illuminating the developed film with a reference beam. Point sources at the object form Fresnel zone plates on the film, which then reform the wavefront under illumination by the reference beam [8].

In digital holography, the film is replaced by an image sensor and the reconstruction process is completed numerically. A recent review is given in [9]. The use of an image sensor brings a number of benefits. First, like in other forms of digital photography, holograms can be recorded and processed in near real time. More important, though, are the benefits of numerical reconstruction. In conventional holography we can use lenses to alter the reconstructed wavefront. In digital holography, such lenses can be implemented numerically.

Since the wavefront is reconstructed in software, digital holography also has direct access to wavefront phase data. Phase data are typically utilized for visualizing transparent objects, such as in phase-contrast microscopy [7], [10] or interferometry through fluids [11]. With digital holograms, conventional flow visualization techniques, such as interferometry, schlieren, and shadowgraph imaging, can all be implemented in software.

Digital holography is an especially powerful technique for dealing with problems where the simultaneous study of small objects and the gas that surrounds them is required. For phenomena like droplet breakup, where multiple small droplets are quickly spread throughout the field of view, digital holography provides the ability to refocus images after collection [12]. At the same time, it provides optical phase information for light transmitted through the surrounding flow.

In this work, holography provides backlit images of solid or liquid objects while simultaneously providing interferometric measurements through the surrounding gas in which the objects are suspended. The interferometric measurements through the gas in the acoustic levitator give the integrated density along the line of sight associated with each image pixel. By assuming that the levitator is axisymmetric, we can infer the pressure and velocity throughout the viewed region. These fields, in turn, are used to calculate the acoustic radiation pressure at the surface of the suspended object. The object position is tracked using its backlit image, reconstructed from these same holograms. As mentioned above, the object shape and its movement can be used to calculate the force on the object for comparison with the optical measurements. For these calculations, the mass of solid samples can be measured with a sensitive balance. The density of a pure liquid sample can be used with its optically measured shape to determine its mass.

B. ACOUSTIC EQUATIONS

Here we will make use of the acoustic equations for a still, lossless fluid where gravity can be neglected [13]:

$$\frac{\partial \rho'}{\partial t} + \rho_0 \nabla \cdot \mathbf{u} = 0 \tag{1}$$

$$\rho_0 \frac{\partial \mathbf{u}}{\partial t} = -\nabla p' \tag{2}$$

where ρ_0 is the density in the undisturbed fluid, ρ' is the density change due to the acoustic disturbance ($\rho = \rho_0 + \rho'$), and p' is the pressure change due to the acoustic disturbance. Since the fluid is assumed to be still, the velocity vector $\mathbf{u}$ is entirely due to the acoustic disturbance so the prime is omitted.

C. ACOUSTIC RADIATION PRESSURE

The average pressure disturbance over a cycle at a fixed point in space, i.e. the mean Eulerian excess pressure $\langle p - p_0 \rangle = \langle p' \rangle$, gives the acoustic radiation pressure experienced by objects in the field. This pressure grows nonlinearly with the field strength [14]. Wang and Lee [14] developed the following expression for the mean excess pressure by accounting for the nonlinear relationship between the fluid thermodynamic properties:

$$\langle p - p_0 \rangle = \frac{1}{2\rho_0 c_0^2} \left\langle p'^2 \right\rangle - \frac{1}{2} \rho_0 \langle \mathbf{u} \cdot \mathbf{u} \rangle \tag{3}$$

where c_0 is the speed of sound in the undisturbed fluid. This equation is applicable to open systems, like the acoustic levitator employed here. In this work, we utilize measured pressure disturbances and calculate velocities using linear acoustics in order to apply (3) to find radiation pressures.

D. PRIOR WORK

There have been a number of prior studies that have employed optical techniques to measure or visualize acoustic fields. Many of the early works utilized diffractive effects, where multiple waves in the acoustic field act as a diffraction grating, or refractive effects, where the local variations in refractive index act as a lens. Breazeale and Hiedemann [15] compared three techniques, including diffractive measurements and two variants of refractive slit broadening. At the same time, researchers employed schlieren techniques, which are commonly used in gas dynamics measurements, to visualize and quantitatively measure acoustic fields. Schlieren continues to prove useful in acoustic studies, as is evident from [16]–[21].

With the development of lasers and the corresponding expansion of holography, it and other interferometric techniques were applied to acoustic fields. For example, Alippi and Palmieri used holography to determine the standing-wave-ratio in a 3.5 MHz ultrasound field [22]. Higgins *et al.* [23] performed interferometric displacement measurements on a metallized pellicle in an ultrasonic field to

measure that field in water. Rustad and Morset [24] utilized a holographic method to determine the acoustic field produced by a loudspeaker. Yuldashev *et al.* [25] utilized a Mach-Zehnder interferometer to measure the profile of a spherical shock produced in air by a spark.

These last two references also utilized tomography to reconstruct the three-dimensional field from line-of-sight measurements through the region of interest [24], [25]. We utilize tomography in this work, assuming that the field of interest is axisymmetric. Tomography has also been used in some of the schlieren studies mentioned above to reconstruct the acoustic field [20], [21].

A particular interferometric technique that has been utilized by a number of researchers in acoustics is laser Doppler velocimetry (LDV). This technique is more typically used to monitor vibrations at a point on a surface. Laser light is reflected from the surface and allowed to interfere with a reference beam from the same laser. Displacement of the surface causes the phase of the reflected light to vary, so displacements or vibrations can be readily measured.

When used in acoustic studies, the measurement beam is often reflected back into the system by a fixed mirror. The same beam is also allowed to pass through the acoustic field. The apparent velocity signal can then be related to changes in the index of refraction associated with the field. Scanning the beam allows an image of the field to be gathered.

Jia *et al.* [26] used this configuration to measure the acoustic pressure, integrated along lines of sight, for pulsed ultrasound in water and air. Torras-Rosell *et al.* [27] used the same configuration to look at audible frequencies in air, reconstructing the field using tomography.

Laser Doppler velocimetry has also been applied to acoustic levitation systems. Koyama and Nakamura [28] used the technique with a scanning system to visualize index variations in an acoustic levitation system designed to transport particles. Seah *et al.* [29] applied scanning LDV to monitor the pressure in an acoustic levitator/manipulator arrangement consisting of eight ultrasonic emitters. Andrade *et al.* [30] used LDV to visualize the field in a single-axis acoustic levitator and examine nonlinear effects. They looked at fields at the drive frequency of the ultrasound and its harmonics to examine harmonic generation.

Interferometric techniques that respond directly to optical phase variations, like holography and laser Doppler velocimetry, can, in many ways, be considered equivalent. Their differences lie in the way that their phase data are sampled in time and space. In scanning LDV systems, high-bandwidth measurements can be made for a single line of sight, but simultaneous measurements at different locations in space are not possible. In pulsed digital holography, measurements are simultaneous in space, but the bandwidth is limited by the frame rate of the camera.

For this work, the simultaneous spatial information allows us to track the movement and shape of levitated objects and to refocus as necessary. We are not able to sample at the ultrasound frequency while still collecting full-frame images, but we are able to synchronize with the ultrasound drive in order to track the acoustic signal. Further details are given below.

Finally, we mention two prior studies where holography has been used to examine acoustic levitation. Zhao *et al.* [31] demonstrated digital holography of acoustic levitation in a configuration similar to ours. Images presented in their paper showed how the acoustic field changed once an object was levitated. Earlier, Leung and Wang [32] had utilized conventional holography to visualize interactions between thermal disturbances and acoustic streaming for a heated sphere in a standing wave.

Although a number of prior studies have performed quantitative measurements of the acoustic field, we are not aware of any that directly applied optical results to calculate forces on levitated objects in these fields. Using the optical results in this way is expected to be more challenging than calculating the local acoustic pressure values, since the presence of the surface means that we are looking toward an interface where diffraction, viscous effects, and spatial resolution may affect the results.

Note also that our calculations do not utilize simulation results in conjunction with the experimental measurements. We wanted to leave the technique as general as possible in order to explore deviations from simulated behavior.

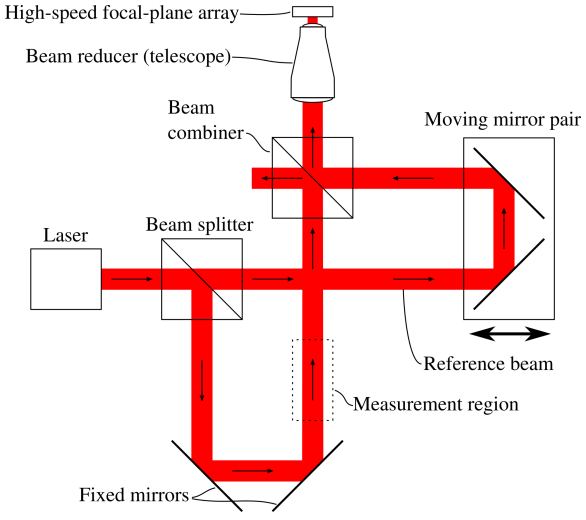

FIGURE 1. Optical configuration used for digital holography.

III. EXPERIMENTAL SETUP

A. OPTICAL CONFIGURATION

The optical configuration for the experiments is shown in Fig. 1. The optical arrangement is a Mach-Zehnder interferometer. The arrangement used here is similar to that used in our previous study [33]. Collimated light from a pulsed 905 nm semiconductor laser passes through a cube beam splitter, forming a measurement (object) beam and a reference beam. The measurement beam is folded back with a pair of fixed mirrors, leaving space for the acoustic levitator.

The levitator is placed so that the measurement beam passes through its acoustic resonator in the area labeled "measurement region." The acoustic field and suspended object are measured in transmission. This arrangement provides backlit images of the object, making it appear mostly dark on a light background.

The reference beam is folded back by a pair of mirrors mounted on a linear stage. The linear stage allows the total path length in the measurement and reference arms to be matched. This matching is necessary because of the short coherence length of the pulsed laser.

When the path lengths are nearly matched, interference fringes form on the focal-plane array. Though it is not immediately evident in the diagram, the mirrors can be adjusted in position and orientation so that there is an angle between the measurement beam and the reference beam when the two overlap on the array. This angle produces an angular separation between the reconstructed measurement beam, its twin, and the zero-order beam. Spatial filtering [8] is then performed during the reconstruction to eliminate the twin and zero-order beams.

For the measurements reported here, the laser was an OSRAM Opto Semiconductors 905 nm, 25 W Pulsed Laser Diode, model SPL PL90 driven by a pulse-forming network. In order to sample as much of the acoustic resonator volume as possible, the bare laser output was allowed to expand to a diameter greater than 25 mm and then collimated with a cemented doublet. An aperture ahead of the lens limits the beam to a diameter slightly smaller than the one-inch (25.4 mm) diameter optics used throughout the system.

The camera/focal-plane array used in the system is a Photron FASTCAM Mini UX100 high-speed camera. Before reaching this camera, the combined beam passes through a beam reducer, reducing its diameter by a factor of two. This allows the beam to fit onto the focal-plane array. The array consists of 1280 by 1024 pixels, and these pixels are square with 10 μm sides. After passing through the beam reducer, the combined beam is about 2 mm taller than the 10.24 mm-tall array but is contained within its 12.80 mm width.

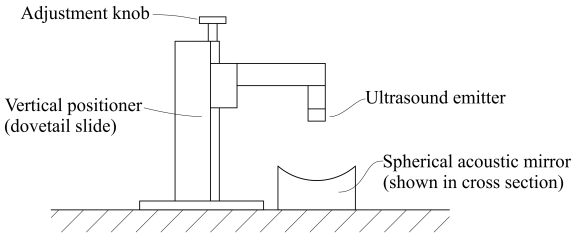

FIGURE 2. Diagram of the acoustic levitator.

B. ACOUSTIC LEVITATOR

A diagram of the acoustic levitator is shown in Fig. 2. It is a single-axis levitator, consisting of an ultrasonic emitter positioned above a spherical acoustic mirror [30]. The emitter is a Murata Electronics model MA40S4S, with a nominal resonant frequency of 40 kHz. The emitter is driven by a variable-voltage DC supply that is modulated by an H-bridge. The H-bridge output is filtered with a passive ladder filter to give a sinusoidal voltage when loaded by the emitter. For the experiments here, the emitter was driven at 40.7 kHz. This value is the measured resonant frequency of the free-standing emitter for ambient temperatures near 25 °C.

The acoustic mirrors used in this work were machined from aluminum, and each featured a spherical concave surface with a radius of curvature of 34.00 mm. This radius corresponds to four wavelengths of 40.7 kHz sound in air at 298 K. Two different mirror diameters were employed. Except for Fig. 3, all of the measurements discussed used a 60 mm diameter mirror. The figure shows data taken with a 44.5 mm diameter mirror.

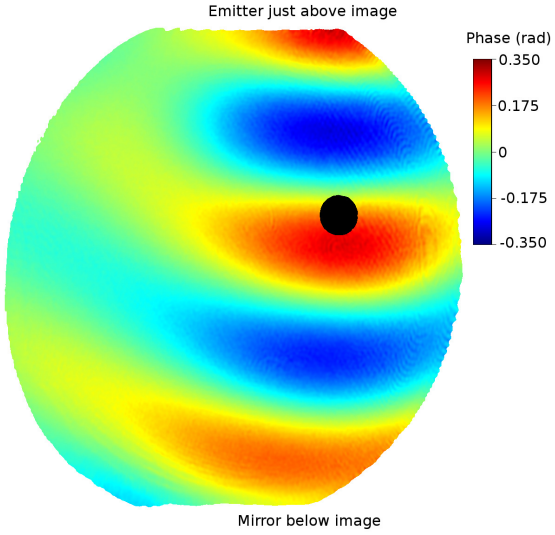

FIGURE 3. Phase image of an acrylic sphere (0.0625in/1.59 mm diameter) suspended in the acoustic levitator. The phase variations are indicative of the integrated refractive index variations along the beam path.

The emitter and mirror combination forms a resonant cavity. Fig. 3 shows optical phase data for a 0.0625 in (1.59 mm) diameter acrylic sphere suspended in the acoustic levitator. The standing wave pattern near the emitter is visible in the figure. The sphere appears near the right side of the image. For this image, the levitator was placed with its axis off center in the measurement beam to capture more of the off-axis field.

The data in Fig. 3 show that the nodes, which appear in light green, have a roughly spherical shape. The suspended object sits below the node so that the net vertical force balances the object's weight.

The vertical placement of the emitter is critical to ensuring that the cavity is resonant. The levitator constructed for this work uses a vertical positioner that is manually adjusted. The spherical mirror is mounted on a two-axis positioner, which is not visible in the diagram. This horizontal positioner allows the mirror to be centered beneath the emitter to ensure an axisymmetric acoustic field.

Although the cavity is resonant, the emitter is smaller than the 8.5 mm ultrasound wavelength and even the diameter of the larger mirror is only 7 times this wavelength. Diffraction therefore allows the field to extend outside of the levitator. In the experiments, care has been taken to minimize reflections from outside objects that would affect the symmetry and performance of the levitator. The wide breadth of the acoustic field requires that we take special steps in its tomographic reconstruction, as is discussed below.

The presence of the levitated object alters the acoustic field in the resonator, as the oscillating flow is forced to move around the object. This change alters the resonant frequency of the cavity, and can lead to levitator instability [4]. For larger objects and flat objects such as discs, the emitter position must sometimes be changed versus its position for small objects to allow their levitation.

In addition to overall changes in the cavity behavior, the presence of the object causes local alterations to the field. For smooth objects, such as the spheres and droplets studied here, the effects blend smoothly with the undisturbed field. For objects with flat faces, localized reflections can be pronounced, producing sharper field gradients within the limits of diffraction.

Finally, in order to regulate the humidity of the air in the acoustic levitator, the whole assembly was placed in a transparent enclosure with removable side panels. The humidity is raised by running a small evaporative humidifier in the enclosure. Humidity has a small effect on the refractive index, but can cause significant changes in the attenuation at ultrasound frequencies [13], [34]. The ambient temperature, pressure, and humidity are monitored by sensors and recorded at the time each holographic high-speed video is collected. These data are used in the calculations described below.

C. HOLOGRAPHIC VIDEO COLLECTION

The high-speed camera is used to collect 12-bit full-frame images at 4050 frames per second. The camera can store 2180 frames in each video segment, corresponding to 0.538 s of data. The frame rate used is about a factor of ten lower than the ultrasound frequency. In order to capture variations in the acoustic field despite this low sampling rate, the laser must be synchronized with the ultrasound drive signal. The laser is pulsed every ten ultrasound cycles, while also being shifted in phase, relative to the ultrasound, at each pulse. The phase shift is chosen to allow a complete cycle of the ultrasound to be captured every 20 frames. With an ultrasound frequency of 40.7 kHz and the phase retardation of $2\pi/20$ with each frame, the laser pulse frequency becomes $f_{\text{laser}} = 4049.75$ Hz. The ultrasound drive and laser trigger signals are derived from a microcontroller hardware timer driven by a crystal-controlled input signal. A camera synchronization signal is also generated by the hardware timer.

The phase-locking approach effectively aliases the high-frequency signal associated with the ultrasound down to an average frequency of $f = f_{\text{laser}}/20 = 202.49$ Hz. The region in the frequency spectrum around 202.49 Hz is reasonably free of narrowband noise. Most of the narrowband noise in the system falls from 20 Hz to 80 Hz.

IV. CALCULATION PROCEDURE

A. DIGITAL HOLOGRAPHY

The hologram reconstructions in this work were performed using the propagation of angular spectrum method [8]. In a given plane with its normal vector in the z direction, the electric field $E(x, y)$ can be spatially Fourier transformed to yield

$$A(f_x, f_y) = \int_{-\infty}^{\infty}\int_{-\infty}^{\infty} e^{-2\pi j(f_x x + f_y y)} E(x, y)\, dx\, dy \qquad (4)$$

where f_x and f_y are the spatial frequencies in the x and y directions. The Fourier decomposition breaks the field in the plane into its component plane waves, each with a unique in-plane direction given by f_x and f_y. Meanwhile, if these waves are propagating in a uniform medium with wavelength λ, the wave vector $k = 2\pi/\lambda$. The wave vector components are $k_x = 2\pi f_x$ and $k_y = 2\pi f_y$ and $k_z = 2\pi f_z$. For a given plane wave with k_x and k_y we can calculate k_z by

$$k_z = \sqrt{k^2 - k_x^2 - k_y^2} \qquad (5)$$

In cases where the in-plane wave vector exceeds the wave vector in the medium, k_z is imaginary and we have an evanescent wave.

To propagate the field to another plane at distance z, we multiply each component plane wave by $\exp(-jk_z z)$ using its particular k_z. As long as the propagation is over a sufficient distance, we simply zero out any evanescent components. At the new plane, we calculate the inverse Fourier transform to recover the electric field.

The digital hologram reconstruction is completed in analogy to the conventional optical reconstruction technique. The intensity variation across the focal plane array is used to amplitude modulate the electric field of a computational reference beam illuminating the array. The electric field (with amplitude and phase) can then be calculated at any other plane by the angular spectrum method. At the desired plane, the light intensity is proportional to the squared magnitude of the calculated field. The phase data for the calculated field are unwrapped to eliminate phase steps at the $-\pi$ and π boundaries.

The reconstruction produces the desired image, a zero-order diffraction term, and a twin image. The off-axis configuration produces angular separation between these images. The zero-order and twin images are suppressed by the spatial filtering technique, where the angular separation is used to remove the unwanted images in the spatial-frequency domain [8], [33].

B. PRESSURE AND VELOCITY FIELD CALCULATIONS

The data used in the calculations begin as a raw binary video file, consisting of a sequence of holograms. These holograms are reconstructed and spatially filtered to generate a series

of phase and intensity image files. Once these images have been generated, the intensity image is used, with an adaptive threshold, to mask the object pixels, and the masked phase data are used in the field calculations.

1) FILTERING

The phase data collected for each frame are indicative of instantaneous variations in the index of refraction along the line of sight for the measurement beam. Tomography is used to reconstruct the radial variation of the index of refraction from the individual pixel phase values by assuming that the system is axisymmetric. These calculations, discussed below, amplify high-spatial-frequency noise in that data. In order to effectively utilize tomography, the phase data must first be filtered.

A major source of noise in the phase data is real variations in phase that are unrelated to the acoustic field. As Fig. 1 suggests, the path length in each arm of the interferometer must be considerably longer than the path through the measurement region. Density variations along the path due to temperature differences are recorded with the acoustic data. These noise sources tend to appear at low frequencies. Overall thermal drift also affects the data, and also appears at low frequencies.

Filtering is accomplished in two steps: individual pixel filtering in time and then radial filtering, in space, at each time. In the first step, the pixels are filtered in time over the full sequence of images. In general, there will be some movement of the object over the image sequence. This movement means that a few of the pixels will have valid phase data for some images and be obscured in others (recall that the backlit object appears mostly dark, so phase data within it are not useful). To avoid these intermittent pixels, each pixel is tracked by its height relative to the measured object centroid and its horizontal distance from the edge of the object. For example, a time sequence might be made up of the phase for the pixel that is five pixels above the centroid and two pixels out from the edge for each time. As the object moves (or even changes shape), the pixel location used in the sequence changes relative to the image.

This tracking approach is expected to produce reasonable results as long as the object is not moving very fast or very far. The object movement introduces a convective term into the phase variation that is being filtered. For the slowly moving objects considered here, the errors associated with this approach are expected to be small. Fast moving objects, which will be considered in future work, may require corrections.

The tracked pixels are filtered in time using a bandpass filter with a 35 Hz bandwidth centered at 202.5 Hz. Data near the beginning and end of the sequence, where wrapping or zero padding would be required, are discarded.

Once the time filtering has been completed, the second step of filtering is applied, at each time, to horizontal lines extending from the edge of the object. Here, the phase data in a given line are fitted with a Fourier cosine series with a small number of terms (we use the symbol β for phase angle):

$$\beta(r) = a_0 + \sum_{n=1}^{M} a_n \cos(2\pi nr/R) \tag{6}$$

where r is the radial distance from the centroid of the object and R is the full period for the fundamental component. In this work, R was set to 1500 pixels and ten cosine terms were used. These choices provided good smoothing performance. The cosine series ensures that the phase function has zero slope at $r = 0$, thereby ensuring that the spatially filtered phase is axisymmetric.

2) TOMOGRAPHY

The optical phase data associated with a given pixel are the result of changes in the index of refraction along the entire line of sight associated with that pixel. In fact, diffraction due to these index variations can cause further complications, with interference from multiple paths removing this simple pixel-to-line-of-sight correspondence [35]. For the measurement geometry considered here and the relatively long ultrasound wavelength used, the assumption of straight paths through the gas only yields small errors. We therefore proceed to recover the local pressure values from the line-of-sight phase data under the assumption that these lines of sight are straight.

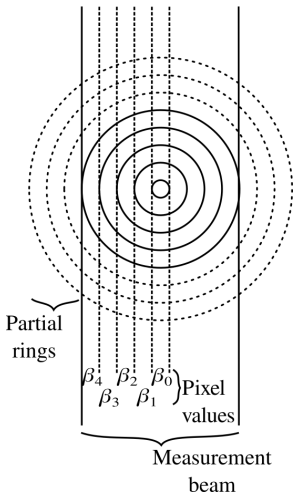

FIGURE 4. Plan-view diagram for a tomography problem with the acoustic field occupying eight rings (each is one-pixel tall and one-pixel thick), but with the measurement beam only covering five of the rings.

We assume that the system is axisymmetric and utilize tomography to recover the radial variation of refractive index from the phase data. A diagram illustrating a tomography problem of this type is shown in Fig. 4. The diagram shows a certain horizontal slice of the axisymmetric acoustic field in plan view, with the measurement beam passing through it. The diagram will be used for some representative calculations below, so we have limited it to eight of the one-pixel-tall and one-pixel-thick "rings" which are each assumed to contain gas of constant refractive index. In an ideal situation,

we would have phase data out to the edge of the refractive index disturbance. Fig. 4, however, allows for the more complicated situation that we encounter in this work, where the acoustic field extends beyond the bounds of the measurement beam. That is, we assume that the field is contained within the eight rings shown, but the measurement beam only encompasses the five inner rings, giving the pixel values $\beta_0, \beta_1, ..., \beta_4$.

For pixel i, the total path length through ring j is given by L_{ij}. The phase disturbance measured for that pixel is then

$$\beta_i = \sum_{j=0}^{7} \frac{2\pi L_{ij}(n_j - n_{\text{ref}})}{\lambda_0} \tag{7}$$

where λ_0 is the vacuum wavelength, n_j is the index of refraction in ring j, and n_{ref} is the index of refraction for the air traversed by the reference beam. If we define $\mathbf{L}$ as the matrix with elements L_{ij}, $\mathbf{b}$ as a vector with components β_i, and we define a vector $\mathbf{g}$ with components $g_j = 2\pi(n_j - n_{\text{ref}})/\lambda_0$, we can write this equation in matrix form:

$$\mathbf{Lg} = \mathbf{b} \tag{8}$$

Here the matrix $\mathbf{L}$ has five rows and eight columns, so the problem is underdetermined.

The problem is underdetermined because the narrow measurement beam gives fewer unique pixel values than there are index values. We refer to the outer three rings, which do not fall completely within the measurement beam, as *partial* rings. We refer to the rings falling completely within the measurement beam as *visible* rings.

TABLE 1. Comparison of the actual field distribution to different tomography solutions for the problem of Fig. 4.

ring	actual	zero assigned	min. norm	min. curvature
0	1.00000	1.00520	0.98365	1.00041
1	0.25000	0.25505	0.23362	0.25043
2	0.11111	0.11886	0.08871	0.11159
3	0.06250	0.06522	0.04729	0.06312
4	0.04000	0.08569	-0.06116	0.04083
5	0.02778	0	0.02919	0.03063
6	0.02041	0	0.08670	0.02042
7	0.01563	0	0.11125	0.01021

One straightforward approach to handling the excess unknowns is to simply assign them each a field value of zero (in which case their values would simply be missing from the analysis). Though simple, this approach is problematic. With this assumption, the calculation assumes that the pixel value β_4 would come entirely from the field in ring 4. However, the portion of the beam associated with β_4 has about twice the path length through the partial rings as it has through ring 4. For a decaying field strength in the rings, the calculation will drive the ring-4 value high. This is illustrated in the calculation given in Table 1. The value for ring 4 is more than double its actual value, and the other rings are all high as well. Another approach would be to include all eight rings in the calculation and compute the minimum norm solution to the resulting underdetermined least-squares problem using singular value decomposition [36]. In this case, also included in Table 1, the value for ring 4 is driven negative, and the partial rings increase toward ring 7, rather than decreasing.

A better approach is to compute the least-squares solution for all eight rings but provide additional constraints that ensure that the partial rings decay toward zero. There is one adjustable parameter for each partial ring. We add one constraint per adjustable parameter by minimizing the finite-difference approximation to the second derivative of the g values with respect to radius at each partial ring. For the outermost ring, we assume the next point out to be zero. For our example, we minimize the sum

$$\sum_{j=5}^{7} \left(2g_j - g_{j-1} - g_{j+1}\right)^2 \tag{9}$$

(using $g_8 \equiv 0$) by adjusting g_5, g_6, and g_7. Minimizing the curvature and fixing the outer point encourage the outside rings to decay smoothly to zero.

The solution for our example case (which we refer to as the minimum curvature solution), is compared with the other cases in Table 1. The solution is much better behaved than the other two. The errors in the first two rings have been reduced by more than a factor of ten.

This minimum curvature approach is used in the tomography calculations for this work. Depending on the location of the levitated object in the image, the number of visible rings varies, but a typical value would be 500 rings. In each case, 200 partial rings were assumed. Tests with the actual experimental data indicate that the radiation force only varies slightly in doubling the number of partial rings to 400.

3) PRESSURE FIELD

The tomography calculations give the index of refraction difference $(n_j - n_{\text{ref}})$ for each ring, based on the pixel phase values and the rings through which the beam passes for that pixel. With the index change in each ring known, the instantaneous pressure in the ring can be calculated by assuming that the acoustic waves are isentropic. We assume that air behaves as a calorically perfect gas with its specific heats fixed at their room temperature values. We also assume that the composition of the air remains constant. If the absolute temperature and pressure in still air are T_0 and p_0, we have

$$\frac{T}{T_0} = \left(\frac{p}{p_0}\right)^{(\gamma-1)/\gamma} \tag{10}$$

where γ is the ratio of specific heats, c_p/c_v. If the equilibrium vapor pressure of water at T_0 is $p_{\text{sat},0}$ and the relative humidity in the ambient is RH_0, the mole fraction of water in the ambient is

$$x_0 = \frac{\text{RH}_0 p_{\text{sat},0}}{p_0} \tag{11}$$

At the new temperature T we have a new value of the equilibrium vapor pressure of water, p_{sat}. If the water mole fraction is assumed fixed (i.e. no condensation), then the new relative humidity is given by

$$\text{RH} = \frac{x_0 p}{p_{\text{sat}}} \tag{12}$$

With the temperature, pressure, and relative humidity known, the index of refraction of the air at these conditions is calculated using the Ciddor equation [37]. The Ciddor equation also accounts for carbon dioxide in the air. In all cases considered here, the mole fraction of carbon dioxide was assumed to be 450 parts per million.

Calculations of this type for typical experimental conditions show that the index of refraction is essentially linear with pressure, even for pressure swings of ± 5 kPa. Therefore, for each experiment the measured conditions are used to calculate the slope $\Delta p/\Delta n$. This slope is used to multiply the Δn value for each ring in order to calculate its pressure value.

4) VELOCITY FIELD

In order to calculate the velocity field, we utilize the acoustic equations and assume that we have time-harmonic pressure and velocity fields. That is,

$$p'(r, z, t) = p'_s(r, z)e^{-2\pi jft} \quad \mathbf{u}(r, z, t) = \mathbf{u}_s e^{-2\pi jft} \tag{13}$$

where f is the ultrasound frequency. We substitute these expressions into (2) to yield

$$\mathbf{u} = \frac{\nabla p'}{2\pi jf\rho_0} \tag{14}$$

The velocity is proportional to the pressure gradient but is 90° out of phase with it.

For this work, we need to find the velocity field at the surface of the levitated object. Given our inviscid analysis, this amounts to determining the velocity just outside the acoustic boundary layer surrounding the object. The velocity there must be parallel to the surface. Equation (14) therefore implies that the gradient normal to the surface must be zero. Moving along the surface, we can calculate the derivative of the pressure as we move tangentially. The tangential velocity is then obtained directly from this spatial derivative using (14).

The pressures that we will be differentiating are directly proportional to the index of refraction values obtained through tomography. These values are computed from data along radial lines (horizontal lines in phase images like the one shown in Fig. 3). Noise in the input phase data was filtered *radially* as described above. At this point, we wish to filter across these radial lines to ensure that any noise still present is not amplified by taking the gradient. To provide this filtering and simplify the force calculations, data for the pressure and the two cylindrical coordinates r and z at the surface of the object are fitted as a function of the angle θ measured from the vertical. The geometry is shown in Fig. 5.

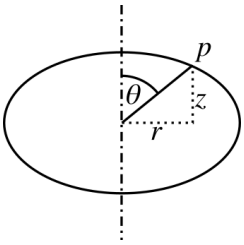

FIGURE 5. Geometry for fitting the pressure and cylindrical coordinates along the object surface.

The quantities p' and z are fitted with a Fourier cosine series, whereas r is fitted with a Fourier sine series:

$$p'(\theta) = \alpha_{p,0} + \sum_{n=1}^{M} \alpha_{p,n} \cos(n\theta) \tag{15}$$

$$z(\theta) = \alpha_{z,0} + \sum_{n=1}^{M} \alpha_{z,n} \cos(n\theta) \tag{16}$$

$$r(\theta) = \sum_{n=1}^{M} \alpha_{r,n} \sin(n\theta) \tag{17}$$

These relationships ensure that r goes to zero at $\theta = 0$ and $\theta = \pi$ and they enforce the periodicity required for properties on the surface.

To calculate the pressure gradient along the surface (moving in the plane of the figure), we use $dp' = (dp'/d\theta)\,d\theta$, $dr = (dr/d\theta)\,d\theta$, and $dz = (dz/d\theta)\,d\theta$. The differential distance traversed along the surface is

$$ds = \sqrt{(dr)^2 + (dz)^2} \tag{18}$$

so

$$\frac{dp'}{ds} = \frac{dp'/d\theta}{\sqrt{(dr/d\theta)^2 + (dz/d\theta)^2}} \tag{19}$$

Using (14), we can write the magnitude of the velocity as

$$|u| = \frac{1}{2\pi f\rho_0}\left|\frac{dp'}{ds}\right| \tag{20}$$

C. FORCE CALCULATIONS

We calculate the radiation pressure at the surface using (3) with the fitted series for $p'(\theta)$ and the velocity calculated from (20). For a truly stationary object, the time averages in (3) can be calculated at each point along the surface over several periods before calculating the force. Here, we allow for slow movement of the object, so we calculate the force over the entire object and then average this force over time. That is, where $\langle p'^2\rangle$ appears in the expression, we simply use p'^2 and average the result after the integration over the surface is completed.

We integrate the vertical force due to pressure over the surface of the object. For axisymmetric objects, we can express the force integral as

$$\langle F_z\rangle = \int \langle p - p_0\rangle\, dA \tag{21}$$

where dA represents the change in cross sectional area as we move along the axis of symmetry (e.g. see [38]). The integral is computed numerically using the radiation pressure and the cross-sectional area computed from $r(\theta)$.

D. BROKEN SYMMETRY

One of the main difficulties with the approach described here is the assumption of symmetry. There is inevitably some movement of the levitated object during the measurement. If that movement includes any horizontal component, the symmetry of the system is broken. More importantly, we have found that the phase data often show asymmetry in the acoustic field, even in the absence of a levitated object. Discussion of possible sources of the asymmetry will be given below. For now, we discuss our simple approach for dealing with the broken symmetry when presenting the experimental results.

In the tomography calculations, note that phase data are only utilized on one side of the levitated object (see the pixel locations in Fig. 4). With perfect symmetry, calculations from the opposite side would yield identical results. Here, we intentionally center the field in the measurement beam so that we can perform force calculations on both sides. We then average the two force values to obtain our result. As we show below, this approach works reasonably well.

A more rigorous approach would be to compute the tomography with the measured asymmetry incorporated. For example, each ring could incorporate variation with azimuth. We will examine this approach in our future work.

V. RESULTS

Data were collected for five varieties of polymer spheres, made of three different materials. For spheres that are small compared to the sound wavelength, the levitation force provided by a plane standing wave is proportional to the sphere volume and the square of the pressure amplitude [14]. The ability of the levitator to support a particular sphere at a given field strength therefore depends primarily on the sphere density. We therefore tested materials of different densities. For the solid spheres, we utilized nylon (density 1.14 g/cm^3), acrylic (1.21 g/cm^3), and Delrin® acetal (1.41 g/cm^3). For all three materials, we tested 0.0625 in (1.59 mm) diameter spheres. For the nylon and acetal, we also tested larger spheres, of 0.0938 in (2.38 mm) diameter. We chose the materials because they were available in the 1.59 mm size with tight tolerances. This size was the smallest diameter available from the supplier we used.

As the technique developed here is meant for the study of liquid droplets, we also collected data on the evaporation of distilled water droplets. With the water it is not possible to weigh the sample at each time. However, given the ambient humidity and temperature, the droplet density can be estimated and used with the optically measured volume to compare with the force.

For each of the solid spheres, ten high-speed video segments were collected at similar conditions. For each segment, we calculated the cycle-averaged force as a function of time. The cycle-averaged force was computed by calculating the force for each frame and then performing two passes of a 20-point running average.

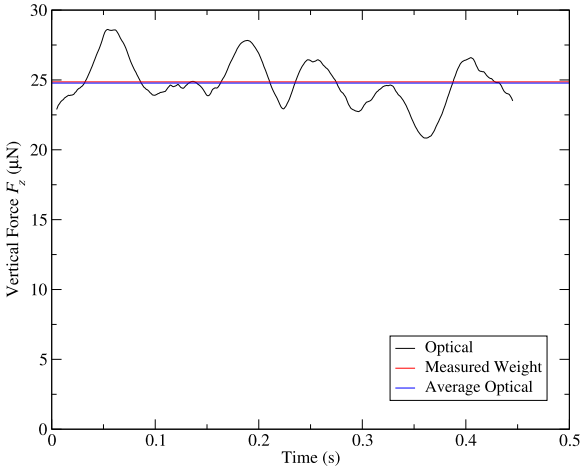

FIGURE 6. Optically measured force data for one high-speed video segment of the 1.59 mm-diameter acrylic sphere. Also shown are the average of the optical data and the measured weight of the sphere.

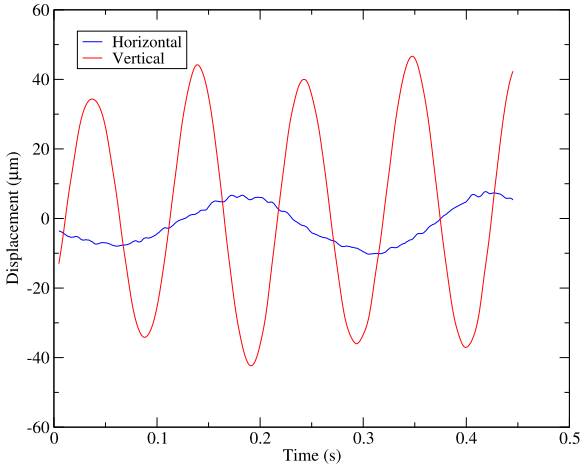

FIGURE 7. Displacement of the sphere centroid for the 1.59 mm-diameter acrylic sphere case examined in Fig. 6.

Force data for one high-speed video segment of the 1.59 mm-diameter acrylic sphere are shown in Fig. 6. Also shown are horizontal lines for the average of the optical force data and for the measured weight (24.9 μN) of the sphere. The average is in good agreement with the measured weight for this case, but we see fluctuations in the measured force over time. For this case, the force reaches a high value of 28.6 μN and a low value of 20.8 μN. The measured displacement of the sphere centroid is shown in Fig. 7. The sphere exhibits small oscillations in the vertical and horizontal directions. The frequency of vertical oscillations is typically higher than that of the horizontal oscillations, because the effective spring constant produced by the acoustic field in the vertical direction is greater.

Generally, we have found that there is little correlation between the force fluctuations and the object movement in these experiments. The vertical force should include the ma_z component and is therefore expected to vary when there is vertical movement. This variation is small compared to the observed fluctuations, however. The fluctuations are thought to primarily result from refractive-index variations occurring throughout the optical system as a result of thermal drafts. The nature of the fluctuations is discussed in more detail below.

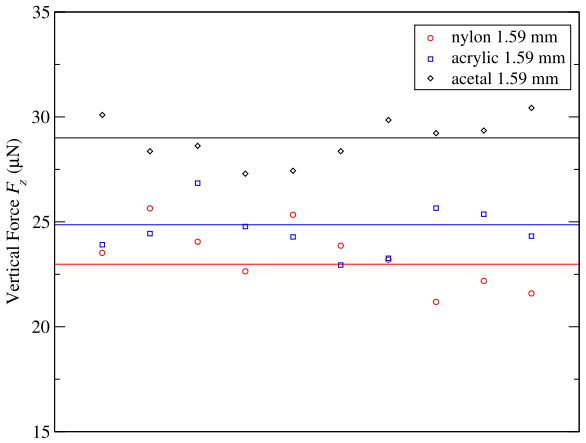

FIGURE 8. Comparison of the average vertical force measured over each high-speed video segment to the measured weight of the sample for the 1.59 mm-diameter spheres.

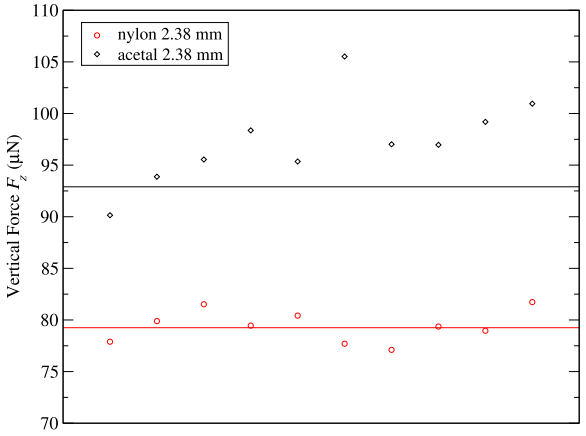

FIGURE 9. Comparison of the average vertical force measured over each high-speed video segment to the measured weight of the sample for the 2.38 mm-diameter spheres.

The average force values from each of the ten video segments and for each of the five samples are compared to the measured weights in Fig. 8 and Fig. 9. In each case, the data were taken sequentially over the course of several minutes. The segment averages show some scatter, but, with the exception of the 2.38 mm-diameter acetal sample, they appear to fluctuate about the measured value rather than drifting off over time. We will see below that the overall average is in good agreement with the measured values for all but the 2.38 mm-diameter acetal sample.

TABLE 2. Comparison of overall average of the measured vertical acoustic radiation force to measured weights for levitated spheres.

Material	Diameter (in/mm)	Radiation Force (μN)	Measured Weight (μN)
nylon	0.0625/1.59	23.3 ± 1.1	23.0
acrylic	0.0625/1.59	24.6 ± 0.8	24.9
acetal	0.0625/1.59	28.9 ± 0.8	29.0
nylon	0.0938/2.38	79.4 ± 1.1	79.3
acetal	0.0938/2.38	97.3 ± 3.0	92.9

For that acetal sample, the data appear to drift upward with successive samples and the sixth point is considerably higher than the rest. The main difference between this case and the others was that it required a significantly higher power input to the emitter to levitate the sample. Once again, the suspected cause is thermal currents affecting the phase measurements.

The overall averages (each being the average of the video-segment averages for a given sphere) are tabulated in Table 2. This table includes an uncertainty in the overall average (rather than an uncertainty for the individual segment averages), calculated for a 95% confidence interval using Student's t distribution. For all but the 2.38 mm-diameter acetal sample, the overall average agrees with the measured weight within experimental uncertainty. For that acetal sample, the results are biased but the overall average is still only 4.7% high.

Note that the uncertainties for the overall average are all around ± 1 μN, except for the 2.38 mm-diameter acetal sample. A ± 1 μN uncertainty corresponds to a segment-average uncertainty of ± 3.2 μN. Reference to Fig. 9 indicates that the increased uncertainty for the large acetal sample is in part the result of assuming that the segment averages are identically distributed when there is actually an upward trend.

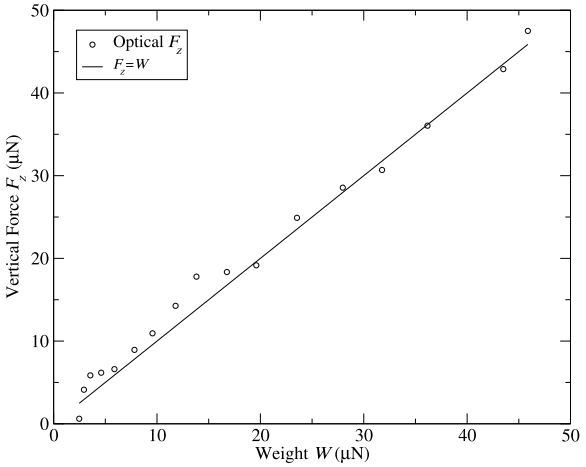

FIGURE 10. Comparison of optically measured vertical force to droplet weight during the evaporation of distilled water.

Finally, the results for distilled water evaporation are shown in Fig. 10. The optically measured vertical force is

plotted versus the droplet weight for water evaporation in air at 24.5 °C with a relative humidity of 68%. The weight is calculated from the droplet volume, using the density for water at the wet-bulb temperature corresponding to those conditions. The volume is calculated from the droplet shape in the reconstructed holograms, assuming that the droplet is axisymmetric. The fitted data for the cylindrical coordinates r and z used in the force calculations are also used here.

The plot also includes the line corresponding to $F_z = W$. The optical force data agree reasonably well with the weight. For the 17 points, the maximum observed error was 4.0 μN for a weight of 13.8 μN.

VI. DISCUSSION

The results presented above show that the method developed here can determine object weights to about ±3.2 μN from 0.5-second segments of video. This precision may be enough for some applications, where samples of unknown density are formed. However, our original goal was to determine the forces with enough precision to reconcile the motion of the sample with the measured forces. Achieving this goal will require an order-of-magnitude reduction in the force uncertainty for samples of this size. We therefore look at sources of error in the measurement and discuss how they can be reduced.

There are two important effects that have not been taken into account in the analysis above: acoustic streaming and temperature variations. To better understand the effects of streaming in the experiments, the flows in the acoustic levitator were visualized using theatrical fog illuminated by a laser sheet. Velocity measurements were also made using a hot-wire anemometer. During the fog measurements, the overall flow was found to be asymmetrical, with a vortex appearing to one side of the levitator axis. Near the emitter, where the velocity was highest (confirmed by anemometer measurements), the flow field was consistent. In regions away from the emitter, however, the flows were strongly influenced by thermal currents from the fog generator.

Streaming is responsible for a number of effects observed in the experiments, including rotation of the samples and at least part of the asymmetry. It is not, however, believed to provide a significant contribution to the force on the levitated samples here. Peak velocities of 0.32 m/s were measured just below the emitter. If the 2.38 mm sphere were in a steady flow of this velocity, the drag would be 0.41 μN. Given that the samples are levitated in an area where the streaming velocity is lower, the force is expected to be below our threshold of detection. Indeed, the overall average data in Table 2 indicate that this is the case for all but the larger acetal sphere. We believe that the conclusion holds even in that case.

Temperature variations, however, will now be shown to have a significant effect on the results. The ultrasonic emitter, which is usually just outside the field of view in the measurements, gets considerably warmer than the ambient air. Given the geometry, we would initially expect the warm air surrounding the emitter to be convected upward and out of the beam path. However, the warm air around the piezoelectric element itself can only exit through the front grid of the enclosed emitter. Streaming currents near the emitter must form a recirculating pattern, given that mass can only pass through this grid. The streaming serves to draw cooler, room-temperature air into the emitter while expelling warm air into the levitator.

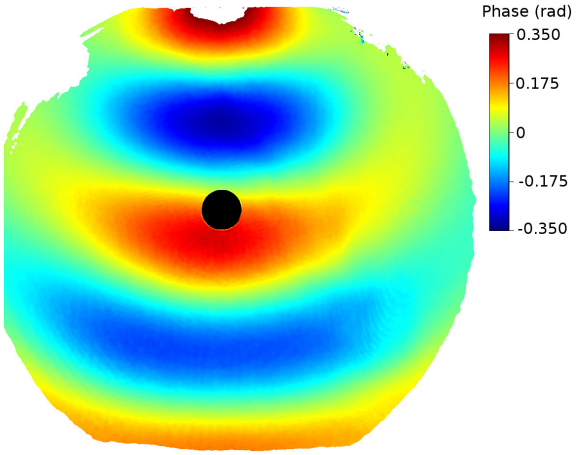

FIGURE 11. Phase image of a nylon sphere (0.0625 in/1.59 mm diameter) suspended in the acoustic levitator.

It is possible to visualize this process using the phase data generated by the digital holography system. Ordinarily, the filtered phase data are dominated by the presence of the acoustic field. Fig. 11 shows optical phase data for a 0.0625 in (1.59 mm)-diameter nylon sphere suspended in the acoustic levitator for a frame where the acoustic pressure is peaking. To remove the acoustic field from the phase data, we perform a principal components analysis on sixty frames chosen from the high-speed video segment. The first two or three whole-image principal vectors obtained in this way are associated with the acoustic field. Thus, the projection of the phase data on each of these image vectors varies sinusoidally with a period of 20 frames. Eliminating these components from each frame allows us to see other processes that might be taking place. Fig. 12 shows the phase data from Fig. 11 with the first three principal components removed, emphasizing the thermal disturbances. Note the change in scale for the phase angles.

There is a streak of thermal ''ripples'' extending down from the emitter and to the right. The emitter is located just above the top center of the image. We have chosen a particularly strong example, where the drive to the emitter was stronger than necessary and the stream of ripples did not get convected much to the right. Often, the ripples can only be seen crossing the top right corner of the image. Movement to the right corresponds with movement toward the vertical positioner shown in Fig. 2.

When we first encountered these ripples, we thought that they might be short-wavelength acoustic waves (they sometimes appear far less sheared than those near the

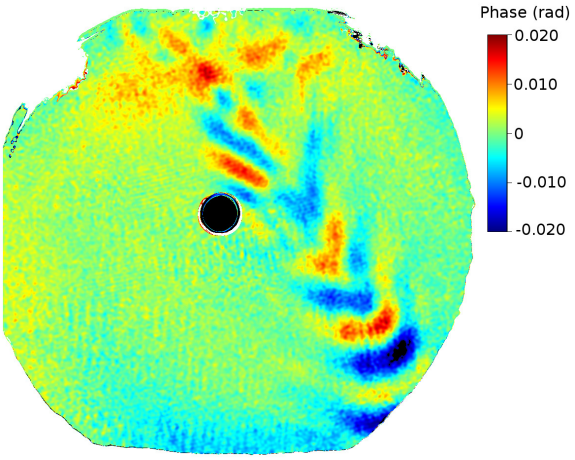

FIGURE 12. Phase image of a nylon sphere (0.0625 in/1.59 mm diameter) suspended in the acoustic levitator with the first three principal components removed to emphasize the thermal disturbances. This is the same frame shown in Fig. 11.

sphere in the figure, so they could be mistaken for waves). Watching the ripples over a series of frames shows that they are convected by acoustic streaming. Velocities determined by tracking the ripples are close to those observed in the streaming experiments discussed above. Thermistor measurements confirm that the average temperature is elevated below the emitter and to the right.

The ripples appear to be generated by the unsteady nature of heat transfer from the emitter. The particular emitter used here employs a cone to improve the impedance match between a piezoelectric bender and the air. The ripple size is about the same as the gap between the outer edge of the cone and the surface of the bender. The ripples were found even in experiments where the emitter was operated with its protective cover removed.

The bias in the results for the large acetal sample and the fluctuations present in all of the data are believed to result from thermal disturbances throughout both beam paths in the optical system. Thermal ripples from the emitter are present in all of the data and become stronger in those cases where a higher emitter drive power was required. The closer the ripples come to the levitated object, the greater is the level of fluctuations found in the force calculations.

While it would be possible to eliminate the disturbances shown in Fig. 12 by utilizing the principal-component data, there are other disturbances of thermal nature that are more difficult to visualize and counteract. Small, moving phase disturbances like those in the figure will appear separately in the principal component data. Likewise, image-wide phase shifts due to thermal drift are filtered out as the phase data are processed. The difficulty lies in intermediate cases. Slow-moving disturbances that cause phase variations across the image are the most difficult to detect and eliminate.

In future work, we plan to carefully examine thermal currents in the optical beam path and work to suppress or homogenize these in order to improve the measurement technique presented here. In addition, we have already had some success with the well-established practice of using porous screens to block streaming flows while allowing acoustic waves to pass. Early experiments show that we can use these screens to keep thermal ripples like those in Fig. 12 from entering the beam path.

VII. CONCLUSIONS

In this work, we utilized pulsed digital holography to determine the acoustic radiation force on objects suspended in a single-axis acoustic levitator. Digital holography provided both the object images and the optical phase data required to determine the instantaneous acoustic pressure. The phase data were utilized in tomography calculations to convert the line-of-sight measurements to a pressure field by assuming that the system was axisymmetric. The pressure field was used to calculate the velocity field and these together were used to calculate the acoustic radiation pressure. This pressure was integrated over the surface of the object to determine the vertical force on the object.

Force measurements were completed for five different polymer spheres, of different sizes and densities, and for an evaporating water droplet. Force data were generated for 0.5-second segments of high-speed video. For the most of these segments, the average force over the 0.5 seconds was determined to within ± 3.2 μN with 95% confidence. Overall average force values were calculated with ten such segments for the polymer spheres.

For all but the heaviest sphere, the overall average of the optically measured force agreed with the measured weight of the sphere within experimental uncertainty. For the heaviest sphere, the overall average was biased upward but was still only 4.7% high. For the water data, the optically measured force was consistent with the droplet volume as the droplet evaporated.

Errors in the measurements have been traced to thermal disturbances in the beam paths of the optical system, and measures have been proposed to reduce these errors in future work.

ACKNOWLEDGMENT

This work included important contributions from a number of undergraduate and graduate students at New York Institute of Technology. In particular, the experimental apparatus and techniques described here were designed and constructed with the help of Archernar Yepes, Jonathan Furniss, Alexander Sooko, Jonas Veloso, and Vaibhav Madhukar Patil. The author is very grateful for their support and enthusiasm.

REFERENCES

[1] J.-K. Park and P. I. Ro, "Noncontact manipulation of light objects based on parameter modulations of acoustic pressure nodes," *J. Vib. Acoust.*, vol. 135, no. 3, 2013, Art. no. 031011.

[2] C. Demore *et al.*, "A sonic screwdriver: Acoustic angular momentum transfer for ultrasonic manipulation," in *Proc. IEEE Int. Ultrason. Symp.*, Oct. 2011, pp. 180–183.

[3] M. A. B. Andrade, F. Buiochi, S. Baer, C. Esen, A. Ostendorf, and J. C. Adamowski, "Experimental analysis of the particle oscillations in acoustic levitation," in *Proc. IEEE Int. Ultrason. Symp.*, Oct. 2012, pp. 2006–2009.

[4] J. Rudnick and M. Barmatz, "Oscillational instabilities in single-mode acoustic levitators," *J. Acoust. Soc. Amer.*, vol. 87, pp. 81–92, Jan. 1990.
[5] R. E. Apfel and J. P. Harbison, "Acoustically induced explosions of superheated droplets," *J. Acoust. Soc. Amer.*, vol. 57, pp. 1371–1373, Jun. 1975.
[6] T. Yoshida and K. Takayama, "Interaction of liquid droplets with planar shock waves," *J. Fluids Eng.*, vol. 112, no. 4, pp. 481–486, 1990.
[7] C. J. Mann, L. Yu, C.-M. Lo, and M. K. Kim, "High-resolution quantitative phase-contrast microscopy by digital holography," *Opt. Express*, vol. 13, no. 22, pp. 8693–8698, 2005.
[8] M. K. Kim, *Digital Holographic Microscopy*. New York, NY, USA: Springer, 2011.
[9] P. W. M. Tsang and T.-C. Poon, "Review on the state-of-the-art technologies for acquisition and display of digital holograms," *IEEE Trans. Ind. Informat.*, vol. 12, no. 3, pp. 886–901, Jun. 2016.
[10] M. K. Kim, L. Yu, and C. J. Mann, "Interference techniques in digital holography," *J. Opt. A, Pure Appl. Opt.*, vol. 8, no. 7, pp. S518–S523, 2006.
[11] D. Igra and K. Takayama, "Experimental investigation of two cylindrical water columns subjected to planar shock wave loading," *J. Fluids Eng.*, vol. 125, no. 2, pp. 325–331, 2003.
[12] D. R. Guildenbecher *et al.*, "kHz rate digital in-line holography applied to quantify secondary droplets from the aerodynamic breakup of a liquid column in a shock-tube." in *Proc. 54th AIAA Aerosp. Sci. Meeting*, Jan. 2016, pp. 1–10.
[13] J. Lighthill, *Waves in Fluids*. Cambridge, U.K.: Cambridge, 1978.
[14] T. G. Wang and C. P. Lee, "Radiation pressure and acoustic levitation," in *Nonlinear Acoustics*, M. F. Hamilton and D. T. Blackstock, Eds. Melville, NY, USA: Acoustical Society of America, 2008, ch. 6, pp. 177–205.
[15] M. A. Breazeale and E. A. Hiedemann, "Optical methods for the measurement of the sound pressure in liquids," *J. Acoust. Soc. Amer.*, vol. 31, no. 1, pp. 24–28, 1959.
[16] W. G. Neubauer and L. R. Dragonette, "A schlieren system used for making movies of sound waves," *J. Acoust. Soc. Amer.*, vol. 49, no. 2A, pp. 410–411, 1971.
[17] W. E. Moore and J. A. Bucaro, "Measurement of acoustic fields using schlieren and holographic techniques," *J. Acoust. Soc. Amer.*, vol. 63, no. 1, pp. 60–67, 1978.
[18] L. Carpenedo, P. Ciuti, and G. Iernetti, "Schlieren optical filtering for sound-intensity measurements," *J. Acoust. Soc. Amer.*, vol. 67, no. 6, pp. 2106–2107, 1980.
[19] "Optical measurement of sound pressure," *J. Acoust. Soc. Amer.*, vol. 87, no. 4, p. 1816, 1990, doi: 10.1121/1.399381.
[20] M. M. Karzova, P. V. Yuldashev, V. A. Khokhlova, S. Ollivier, E. Salze, and P. Blanc-Benon, "Characterization of spark-generated n-waves in air using an optical schlieren method," *J. Acoust. Soc. Amer.*, vol. 137, no. 6, pp. 3244–3252, 2015.
[21] Z. Xu, H. Chen, X. Yan, M.-L. Qian, and Q. Cheng, "Three-dimensional reconstruction of nonplanar ultrasound fields using Radon transform and the schlieren imaging method," *J. Acoust. Soc. Amer.*, vol. 142, no. 1, pp. EL82–EL88, 2017.
[22] A. Alippi and L. Palmieri, "Standing-wave-ratio determination of an ultrasonic wave by a holographic method," *J. Acoust. Soc. Amer.*, vol. 46, no. 5B, pp. 1121–1127, 1969.
[23] F. P. Higgins, S. J. Norton, and M. Linzer, "Optical interferometric visualization and computerized reconstruction of ultrasonic fields," *J. Acoust. Soc. Amer.*, vol. 68, pp. 1169–1176, Oct. 1980.
[24] R. Rustad and L. H. Morset, "Investigation of the near field of a loudspeaker using tomographic reconstruction from tv-holography measurements," *J. Acoust. Soc. Amer.*, vol. 104, no. 3, pp. 1503–1508, 1998.
[25] P. Yuldashev, M. Karzova, V. Khokhlova, S. Ollivier, and P. Blanc-Benon, "Mach–Zehnder interferometry method for acoustic shock wave measurements in air and broadband calibration of microphones," *J. Acoust. Soc. Amer.*, vol. 137, no. 6, pp. 3314–3324, 2015.
[26] X. Jia, G. Quentin, and M. Lassoued, "Optical heterodyne detection of pulsed ultrasonic pressures," *IEEE Trans. Ultrason., Ferroelectr., Freq. Control*, vol. 40, no. 1, pp. 67–69, Jan. 1993.
[27] A. Torras-Rosell, S. Barrera-Figueroa, and F. Jacobsen, "Sound field reconstruction using acousto-optic tomography," *J. Acoust. Soc. Amer.*, vol. 131, no. 5, pp. 3786–3793, 2012.
[28] D. Koyama and K. Nakamura, "Noncontact ultrasonic transportation of small objects over long distances in air using a bending vibrator and a reflector," *IEEE Trans. Ultrason., Ferroelectr., Freq. Control*, vol. 57, no. 5, pp. 1152–1159, May 2010.
[29] S. A. Seah, B. W. Drinkwater, T. Carter, R. Malkin, and S. Subramanian, "Correspondence: Dexterous ultrasonic levitation of millimeter-sized objects in air," *IEEE Trans. Ultrason., Ferroelectr., Freq. Control*, vol. 61, no. 7, pp. 1233–1236, Jul. 2014.
[30] M. A. B. Andrade, T. S. Ramos, F. T. A. Okina, and J. C. Adamowski, "Nonlinear characterization of a single-axis acoustic levitator," *Rev. Sci. Instrum.*, vol. 85, no. 4, 2014, Art. no. 045125.
[31] J. Zhao, E. Li, W. Sun, and J. Di, "Applications of digital holography in visualized measurement of acoustic and flow fields," *Proc. SPIE*, vol. 7522, p. 752221, Apr. 2010, doi: 10.1117/12.851688.
[32] E. W. Leung and T. G. Wang, "Force on a heated sphere in a horizontal plane acoustic standing wave field," *J. Acoust. Soc. Amer.*, vol. 77, pp. 1686–1691, May 1985.
[33] J. J. Scire, J. Furniss, J. Mauro, and K. O'Sullivan, "Digital holography with a cell-phone camera module," in *Proc. IEEE Sensors Appl. Symp. (SAS)*, Mar. 2017, pp. 1–6.
[34] A. B. Bhatia, *Ultrasonic Absorption*. Mineola, NY, USA: Dover, 1967.
[35] J. W. Wolf, T. H. Neighbors, III, and W. G. Mayer, "Optical analysis of finite-amplitude ultrasonic pulses," *J. Acoust. Soc. Amer.*, vol. 87, no. 3, pp. 1004–1009, 1990.
[36] C. L. Lawson and R. J. Hanson, *Solving Least Squares Problems*. Philadelphia, PA, USA: SIAM, 1995.
[37] P. E. Ciddor, "Refractive index of air: New equations for the visible and near infrared," *Appl. Opt.*, vol. 35, no. 9, pp. 1566–1573, 1996.
[38] S. Farokhi, *Aircraft Propulsion*, 2nd ed. West Sussex, U.K.: Wiley, 2014.

JAMES J. SCIRE, Jr., received the B.E. degree in mechanical engineering from The Cooper Union for the Advancement of Science and Art, New York, NY, USA, and the M.A. and Ph.D. degrees in mechanical and aerospace engineering from Princeton University, Princeton, NJ, USA. After completing his Ph.D., he worked for Advanced Fuel Research, Inc., developing optical diagnostics and imaging systems for the company's Combustion Monitoring and Control Group. He has been an Assistant Professor with the Department of Mechanical Engineering, New York Institute of Technology, Long Island, NY, USA, since 2013. His research interests include optical sensors, acoustics, combustion, numerical simulation, and optimization.